

This item is likely protected under Title 17 of the U.S. Copyright Law. Unless on a Creative Commons license, for uses protected by Copyright Law, contact the copyright holder or the author.

Access to this work was provided by the University of Maryland, Baltimore County (UMBC) ScholarWorks@UMBC digital repository on the Maryland Shared Open Access (MD-SOAR) platform.

Please provide feedback

Please support the ScholarWorks@UMBC repository by emailing scholarworks-group@umbc.edu and telling us what having access to this work means to you and why it's important to you. Thank you.



Contextual Predictions for the *Parker Solar Probe*. I. Critical Surfaces and Regions

Rohit Chhiber¹ , Arcadi V. Usmanov^{1,2} , William H. Matthaeus¹ , and Melvyn L. Goldstein^{2,3}

¹Department of Physics and Astronomy, University of Delaware, Newark, DE 19716, USA; rohite@udel.edu

²NASA Goddard Space Flight Center, Greenbelt, MD 20771, USA

³University of Maryland Baltimore County, Baltimore, MD 21250, USA

Received 2018 May 30; revised 2019 January 7; accepted 2019 February 8; published 2019 March 14

Abstract

The solar corona and young solar wind may be characterized by *critical surfaces*—the sonic, Alfvén, and first plasma- β unity surfaces—that demarcate regions where the solar wind flow undergoes certain crucial transformations. Global numerical simulations and remote sensing observations offer a natural mode for the study of these surfaces at large scales, thus providing valuable context for the high-resolution in situ measurements expected from the recently launched *Parker Solar Probe* (*PSP*). The present study utilizes global three-dimensional magnetohydrodynamic (MHD) simulations of the solar wind to characterize the critical surfaces and investigate the flow in propinquitous regions. Effects of solar activity are incorporated by varying source magnetic dipole tilts and employing magnetogram-based boundary conditions. An MHD turbulence model is self-consistently coupled to the bulk-flow equations, enabling investigation of turbulence properties of the flow in the vicinity of critical regions. The simulation results are compared with a variety of remote sensing observations. A simulated *PSP* trajectory is used to provide contextual predictions for the spacecraft in terms of the computed critical surfaces. Broad agreement is seen in the interpretation of the present results in comparison with existing remote sensing results, both from heliospheric imaging and from radio scintillation studies. The trajectory analyses show that the period of time that *PSP* is likely to spend inside the $\beta = 1$, sonic, and Alfvén surfaces depends sensitively on the degree of solar activity and the tilt of the solar dipole and location of the heliospheric current sheet.

Key words: magnetohydrodynamics (MHD) – solar wind – Sun: corona – turbulence

Supporting material: animation

1. Introduction

The expansion of the solar corona into interplanetary space was predicted in 1958 by Parker’s classic model (Parker 1958). Soon after, in situ spacecraft measurements (Neugebauer & Snyder 1966) confirmed that the interplanetary region is pervaded by solar plasma flowing at supersonic speed.⁴ Research efforts in the following decades have established that the solar wind is a complex and dynamic system that enters centrally into much of space research and is of relevance to studies of solar, geophysical, and astronomical phenomena. The *Parker Solar Probe* (*PSP*) mission (Fox et al. 2016) was launched on 2018 August 12, with the goal of exploring, for the first time, regions of solar wind that are of crucial importance in establishing the heliosphere. While approaching the Sun closer than any prior spacecraft, *PSP* will provide unprecedented high-resolution measurements of the solar corona and the young solar wind, with the main objectives being discovery of the structure and dynamics of the coronal magnetic field, and the processes that heat and accelerate the wind and accelerate and transport energetic particles. As the *PSP* makes its high-resolution in situ measurements, a knowledge of the large-scale environment within which these observations exist is of vital importance. This global context may be provided by remote sensing (Bird & Edenhofer 1990; Vourlidas et al. 2016) and global simulation. The present work is the first of a series of papers focused on contextual predictions for *PSP* using global simulations of the solar wind.

The transition of the solar corona into the solar wind is accomplished by several dynamical changes in the nature of the flow, regionally organized by magnetic topology and associated factors such as open versus closed connectivity and composition. Regions of fast wind, slow wind, and mixed wind apparently trace different magnetic connectivities and different altitudes (e.g., McComas et al. 2003; Cranmer et al. 2007). In the simplest picture, the inner coronal plasma is magnetically structured, subsonic, and sub-Alfvénic, but as it flows out from the corona into the young solar wind, it evolves into a supersonic and super-Alfvénic flow that is dominated by hydrodynamics. Recent work indicates that this transition may coincide with the onset of large-scale turbulence (DeForest et al. 2016; Chhiber et al. 2018) and mark the outer boundary of a zone of preferential ion heating (Kasper et al. 2017).

Useful markers that characterize this transition are the sonic critical surface, the Alfvén critical surface, and the first $\beta = 1$ surface (the plasma- β is the ratio of gas to magnetic pressure). In particular, when the flow speed u exceeds the Alfvén speed V_A , the magnetic field rigidity can no longer enforce plasma corotation (Weber & Davis 1967) or overcome the differential ram pressure that is due to shearing interactions between neighboring wind streams. And when the plasma- β increases above unity, gradients in the plasma (thermal) pressure may displace the magnetic field, and more isotropic motions are possible (Chhiber et al. 2018). The broad region in which these two crucial conditions ($u > V_A$ and $\beta \sim 1$) are attained becomes, in effect, the region where the corona gradually gives up control of the solar plasma and the kinetic-energy-dominated solar wind emerges as an independent entity. Beyond these regions, the solar wind no longer communicates

⁴ For a recent historical review of the discovery of the solar wind, see Obridko & Vaisberg (2017).

through magnetohydrodynamic (MHD) interactions with the magnetically dominated regions of its origin.

In this work, we employ well-tested global MHD simulations of the solar wind (Usmanov et al. 2014, 2018), which are self-consistently coupled with a turbulence transport model, to study and characterize this region of transitions and to make contextual predictions for the *PSP* mission.⁵ We incorporate the effects of long-term solar variability (e.g., Owens & Forsyth 2013) by varying magnetic source dipole tilts and employing magnetogram-based boundary conditions. The simulation results are compared with a variety of remote sensing observations, demonstrating how the two approaches may be combined to gain insights regarding large-scale heliospheric conditions in this region. Global simulation and remote sensing thus generate mutual support and, in turn, provide valuable context for the finer details that emerge from in situ measurements. Subsequent papers in this series on contextual predictions for *PSP* will focus on turbulence properties along the spacecraft’s trajectory, on modifications of Taylor’s hypothesis for *PSP* (Matthaeus 1997; Klein et al. 2015), and on solar wind azimuthal flow.

The paper is organized as follows. In Section 2 we provide background on critical surfaces and physically distinct regions of the inner wind, discussing recent work that motivates the present study. An overview of the *PSP* trajectory is provided in Section 3, and our solar wind model is briefly described in Section 4. Results are presented in Section 5, including comparisons of model output with remote sensing observations and contextual predictions along the *PSP* trajectory. We conclude with a discussion in Section 6.

2. Theoretical and Observational Background

Two critical points⁶ are frequently discussed within the context of the solar wind: the sonic and Alfvénic critical points, where the flow speed equals the sound speed and the Alfvén speed, respectively. One encounters the notion in even the simplest, spherically symmetric, stationary and isothermal model of the solar wind (e.g., Hundhausen 1972). We briefly review the standard presentation below.

The relevant equations may be derived by assuming an equal number density n of protons and electrons, and an equation of state $P = 2nkT$, where $T = \frac{1}{2}(T_e + T_p)$ is the average of electron and proton temperatures. Mass conservation ($4\pi n r^2 = \text{constant}$), combined with the inviscid momentum conservation equation in a gravitational potential

$$nm u \frac{du}{dr} = -2kT \frac{dn}{dr} - nm \frac{GM_\odot}{r^2}, \quad (1)$$

yields

$$\frac{1}{u} \frac{du}{dr} \left(u^2 - \frac{2kT}{m} \right) = \frac{4kT}{mr} - \frac{GM_\odot}{r^2}. \quad (2)$$

Here, u is the speed of radial expansion, m is the sum of proton and electron masses, k is the Boltzmann constant, G is the gravitational constant, and M_\odot is the solar mass. The right-hand

side of Equation (2) vanishes at the *critical radius* $r_c = GM_\odot m / 4kT$. The left-hand side must also vanish here, for which we must have either a vanishing velocity derivative or $u^2(r_c) \equiv u_c^2 = 2kT/m$. The solutions of Equation (2) have the well-known “X” or *saddle* type of topology (see, e.g., Hundhausen 1972); the solution of physical interest is transonic, with a monotonically increasing velocity that is equal to the sound speed at the critical radius, that is, at the sonic point.

As additional physical effects are added to a solar wind model, the mathematical structure of the equations changes, and with it the nature of the critical point (e.g., Lamers & Cassinelli 1999). For instance, including electrons in a two-fluid model would introduce two sound speeds and two possible critical points. As we will see in Section 5, inclusion of the electron pressure in a two-fluid model shifts the location of the sonic point to a slightly greater heliocentric distance. Therefore, the “singular” aspect of a critical point is of limited physical relevance, and it is questionable whether spacecraft data may be used to localize a definite critical point. Observational and instrumental issues aside, the sharp transitions between regions of interest that emerge in the simplest models will almost certainly become more gradual transitions, or even “fuzzy” or erratic transitions, in the real solar wind that is influenced by three-dimensional (3D) effects, multifluid plasma physics, turbulence, and so on. In the following, we will refer to these transitions as “surfaces” when it causes no confusion, but we remind the reader that in general we intend nonsingular and more gradual transitions (see also DeForest et al. 2018). From a physical perspective, these critical points become critical surfaces in a 3D context and denote transitions between separate regions in the solar wind that are dominated by different physical effects. For instance, counterpropagating Alfvénic fluctuations may effectively generate turbulence in the inner corona (Matthaeus et al. 1999), but above the Alfvén critical surface, the population of inward-propagating modes is diminished (Bruno & Carbone 2013), and Alfvén wave collisions are no longer an efficient mode of turbulence production (Verdini & Velli 2007). The Alfvén surface also effects a separation of coronal regions having different angular flow properties: in the simplest picture, below this surface the torque produced by the magnetic field is sufficiently strong to transfer angular momentum and produce a corotation of the coronal wind with the Sun, while above the critical surface the azimuthal velocity of the solar wind drops rapidly with distance (Weber & Davis 1967).

In addition to the demarcation of different regions by critical surfaces, the general vicinity of the surfaces may be a site of interesting physics, such as enhancement in turbulent fluctuations (Lotova et al. 1985). These surfaces also signify the point beyond which MHD wave modes are unable to communicate upstream, because above the sonic (Alfvénic) critical surface the speed of propagation of information by sonic (Alfvén) modes is smaller than the speed of their advection downstream by the wind. Further, signatures of different coronal and solar phenomena may be evident in the location and morphology of critical surfaces and may manifest in their temporal and spatial variability (Grall et al. 1996; Lotova et al. 1997).

Recent observations by DeForest et al. (2016) and subsequent numerical investigations by Chhiber et al. (2018) provide additional motivation for the present study. Making use of highly processed *STEREO* images from 2008 December, DeForest et al. (2016) found a textural shift in the solar wind flow between heliocentric distances of 20 and 80 R_\odot . The

⁵ Our use of “transition” here should not be confused with the well-known transition region that lies just above the chromosphere (e.g., Cranmer et al. 2007).

⁶ A mathematical discussion of a critical (or equilibrium) point of a system of ordinary differential equations may be found in standard texts (e.g., Boyce et al. 1969).

images revealed that radially aligned, “striated” patterns gave way to more isotropic structures, which DeForest et al. termed “*floculae*,” at distances of a few tens of solar radii. Chhiber et al. (2018) performed global solar wind MHD simulations, representing nominal large-scale solar wind conditions during 2008 December, and superposed plasma- β unity surfaces computed from these simulations on the *STEREO* images. They found that the observed textural shift occurred near the first plasma- $\beta = 1$ surface. The emerging interpretation states that as the solar wind passes into the region where $\beta \equiv 8\pi P/B^2 \geq 1$, mechanical pressure may overcome the organizing influence of the magnetic field B , thus enabling the observed isotropic motions, which may be triggered by hydrodynamic shearing between wind streams (e.g., Roberts et al. 1992). A further point of interpretation, consistent with the one above, is that the *floculae* may be a manifestation of solar wind fluctuations interacting at the largest scales that are causally related through turbulence in the expanding solar wind (Chhiber et al. 2018). The existence of such a maximum length scale of interaction is clear, based on the finite amount of available propagation time, combined with the assumption that the relevant correlations must be produced by signals propagating at MHD speeds.

The Alfvén and $\beta = 1$ surfaces may also be of significance to the phenomenon of preferential ion heating in the solar wind (e.g., Marsch 2006). Recently, Kasper et al. (2017) found evidence for a zone, extending from just above the transition region ($\sim 0.3 R_\odot$) above the coronal base to a distance of tens of solar radii, where α -particles are heated preferentially over protons. The outer boundary of this zone is likely associated with the Alfvén and $\beta = 1$ surfaces. This point will be discussed further in Section 5.

3. Sampling of the Three-dimensional Heliosphere by PSP

The preceding section serves to emphasize the importance and relevance of critical surfaces. Yet, spacecraft missions hitherto have not been able to sample these in situ (prior to *PSP*, the closest heliocentric distance of approach was that of *Helios* at 0.29 au, or $\sim 62 R_\odot$). *PSP* is set to change this by spending “a total of 937 hr inside $20 R_\odot$, 440 hr inside $15 R_\odot$, and 14 hr inside $10 R_\odot$ ” over its 7 yr nominal mission (Fox et al. 2016). The spacecraft will most likely spend a very substantial amount of time under the first $\beta = 1$ surface, which is inferred to lie between 20 and $60 R_\odot$ (DeForest et al. 2016; Chhiber et al. 2018).⁷ According to observations and models (e.g., Mullan 1990; Lotova et al. 1997; Suzuki & Inutsuka 2005; Cranmer et al. 2007; Verdini et al. 2010; Pinto et al. 2011; Oran et al. 2013; DeForest et al. 2014; Pinto & Rouillard 2017; Chhiber et al. 2018; Perri et al. 2018), the Alfvén surface lies between ~ 2 and $30 R_\odot$, and *PSP* could spend a substantial time under this surface as well. The sonic surface may lie below the *PSP*’s lowest perihelion at $9.86 R_\odot$, because coronal models often predict a location of $2\text{--}5 R_\odot$, although these predictions are applicable mainly to coronal hole regions (Kopp & Holzer 1976; Habbal et al. 1995; McKenzie et al. 1995; Giordano et al. 2000; Cranmer et al. 2007; Verdini et al. 2010). At low latitudes, the sonic point may lie as far as $20 R_\odot$ (Lotova et al. 1997). Since the periods in which the spacecraft will probe the regions within these surfaces will be of special

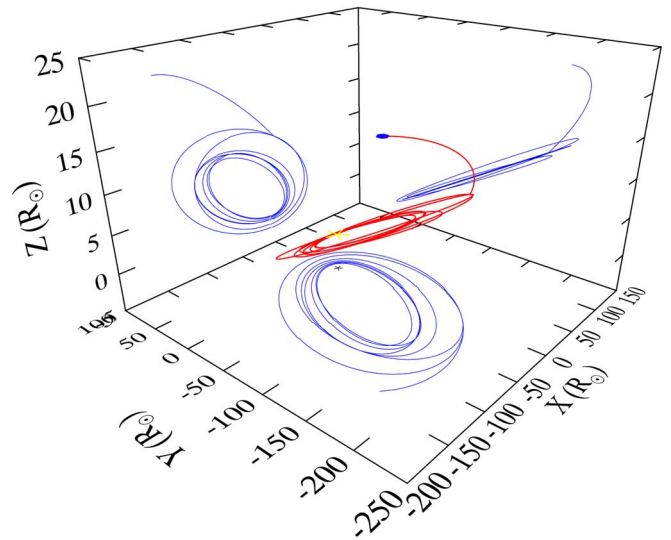


Figure 1. *PSP* trajectory in HCI coordinates (see text for details). The origin is the solar center of mass, and the XY plane is the solar equatorial plane. The red curves show the trajectory in 3D space, and the blue curves are its projections onto the XY , XZ , and YZ planes. The asterisk symbol and blue dot represent the positions of the Sun and Earth, respectively.

significance to the success of the *PSP* mission, it becomes a matter of some importance to estimate when these periods might occur.

Figure 1 shows a 3D perspective of the *PSP* trajectory. The spacecraft ephemeris was extracted from a NASA SPICE kernel,⁸ and the trajectory is presented here in the Heliocentric Inertial (HCI) coordinate system (e.g., Fränz & Harper 2002). Here the XY plane is defined by the Sun’s equator of epoch J2000; the $+Z$ axis is parallel to the Sun’s rotation axis of epoch J2000, pointing toward the Sun’s north pole; the $+X$ axis is the ascending node of the solar equatorial plane on the ecliptic plane of J2000; and the origin of the coordinate system is the Sun’s center of mass. The *PSP* trajectory in 3D space is shown in red, while the blue curves represent projections of the 3D trajectory onto the XY , XZ , and YZ planes. The Earth (at time of launch) and the Sun are represented by the blue dot and the asterisk, respectively (not to scale). The trajectory shown includes all orbits in the 7 yr nominal mission duration.

As *PSP* makes its high-resolution in situ measurements, a knowledge of the large-scale environment within which these observations exist is of vital importance. In the next section, we describe the solar wind model we have used to study the critical surfaces and regions and to make context predictions for the *PSP* trajectory.

4. Solar Wind Model

The large-scale features of the solar wind flow are widely regarded as well represented in a fluid (MHD) description (Goldstein et al. 1995; Tu & Marsch 1995; Bruno & Carbone 2013; Makwana et al. 2015; Matthaeus et al. 2015; Parashar et al. 2015).⁹ The MHD description is particularly

⁷ The location of the Alfvén and first beta-unity surfaces may dip below $10 R_\odot$ at the heliospheric current sheet (HCS). It must be noted that global models are likely to overestimate the spatial extent of the HCS due to their coarse resolution. This issue is discussed further in Section 5.

⁸ <https://naif.jpl.nasa.gov/naif/index.html>

⁹ One objection might be that magnetosonic modes may be heavily damped in kinetic theory (Barnes 1979), an effect absent in MHD. However, compressive modes may represent a small fraction of the energy in the weakly compressive interplanetary medium, and in any case the dissipation rate due to linear damping may be small compared to the cascade rate that leads to turbulent dissipation (Matthaeus et al. 2014).

indispensable for global simulation of the solar wind (e.g., Gombosi et al. 2018), where the largest length scales in the system span at least a few solar radii ($1 R_{\odot} = 6.9 \times 10^5$ km). Kinetic effects come into play near the ion-inertial scale, which is roughly 90 km at 1 au (e.g., Schekochihin et al. 2009) and becomes smaller closer to the Sun. Current and foreseeable computational resources do not permit the resolution of this wide range of scales (e.g., Miesch et al. 2015; Schmidt 2015). This makes MHD simulation our tool of choice for the current study that focuses on the global context of *PSP* observations. However, special provisions need to be made to preserve essential physical information contained in the smaller-scale *fluctuations*, which are necessarily unresolved, even if the macroscopic features are well represented. The large scales traversed by *PSP* orbits are illustrated strikingly in Figure 1, which serves to reinforce the appropriateness of this approach.

Fluid models of the solar wind have adopted various approaches to the problem of incorporating a source of heating and acceleration, including parametric heat deposition (e.g., Habbal et al. 1995; McKenzie et al. 1995; Riley et al. 2015), a polytropic equation of state (e.g., Lee et al. 2009; Gressl et al. 2014), WKB waves in a weakly inhomogeneous background (e.g., Jacques 1978; Usmanov et al. 2000), and MHD turbulence driven by Alfvén waves interacting with large-scale gradients (e.g., Matthaeus et al. 1999; Dmitruk et al. 2002; Suzuki & Inutsuka 2005; Verdini et al. 2010; van der Holst et al. 2014; Yang et al. 2016). We use an approach with a fully self-consistent and dynamical coupling of bulk solar wind flow with small-scale MHD turbulence: bulk flow influences the turbulence, and, in turn, turbulence dynamically feeds back into the bulk wind flow. In addition to turbulent heating and acceleration, the model incorporates two-fluid energy equations, heat conduction by electrons, and proton–electron Coulomb collisions. We briefly describe the model below and refer the reader to Usmanov et al. (2018) for details, including those of the turbulence model and closure approximations.

Formally, the model is based on a Reynolds decomposition (e.g., Monin & Yaglom 1971) applied to MHD. All physical fields, for example $\tilde{\mathbf{a}}$, are separated into a mean and a fluctuating component, $\tilde{\mathbf{a}} = \mathbf{a} + \mathbf{a}'$, making use of an averaging operation where $\mathbf{a} = \langle \tilde{\mathbf{a}} \rangle$. This ensemble average is associated with the large scales of motion, assumed to be deterministic. The quantity \mathbf{a}' is a fluctuating component, here assumed to be of arbitrary amplitude and random in nature. By construction, $\langle \mathbf{a}' \rangle = 0$.

The model assumes that the solar wind is a fully ionized proton–electron plasma. The two species are described as fluids with separate energy equations, and it is assumed that the bulk velocity is the same for the two species (Hartle & Sturrock 1968; Hundhausen 1972; Isenberg 1986; Marsch 2006). The velocity and magnetic fields are Reynolds-decomposed into mean and fluctuating components, $\tilde{\mathbf{v}} = \mathbf{v} + \mathbf{v}'$ and $\tilde{\mathbf{B}} = \mathbf{B} + \mathbf{B}'$, and the decomposed fields are substituted into the momentum and induction equations in the frame of reference corotating with the Sun. The ensemble averaging operator $\langle \cdot \rangle$ is applied, yielding large-scale, mean-flow equations: a continuity equation, a momentum equation, an induction equation, and two pressure equations. The dependent variables are the mean velocity in the corotating frame \mathbf{v} , the mean magnetic field \mathbf{B} , the number density N_S , the pressure P_S of solar wind (thermal) protons, and the pressure of electrons P_E . Pressures are assumed to be isotropic, and we neglect density and pressure fluctuations

(Usmanov et al. 2014, 2018). The mass density $\rho = m_p N_S$ is defined in terms of the proton mass m_p .

We use the classical Spitzer formula (Spitzer 1965; Hartle & Sturrock 1968) for the proton–electron Coulomb collision timescale, and the electron heat flux below $5\text{--}10 R_{\odot}$ is approximated by the classical collision-dominated model of Spitzer & Härm (1953; see also Chhiber et al. 2016), while above $5\text{--}10 R_{\odot}$ we adopt Hollweg’s “collisionless” model (Hollweg 1974, 1976). Four turbulence quantities arise in the mean-flow equations: a source term Q_T of energy deposition/extraction due to turbulent dissipation, the Reynolds stress $\mathcal{R} = \langle \rho \mathbf{v}' \mathbf{v}' - \mathbf{B}' \mathbf{B}' / 4\pi \rangle$, the magnetic pressure of the fluctuations $\langle B'^2 \rangle / 8\pi$, and the mean turbulent electric field $\epsilon_m = \langle \mathbf{v}' \times \mathbf{B}' \rangle (4\pi\rho)^{-1/2}$. These represent the coupling of the bulk flow to the small-scale fluctuations. Transport equations for the fluctuations are obtained by subtracting the mean-field equations from the full MHD equations. This yields a set of equations that describe the transport of three statistical descriptors for solar wind MHD fluctuations—the turbulence energy, the correlation length of turbulent fluctuations, and the cross helicity—which are coupled to the mean-field equations through terms involving Q_T , \mathcal{R} , and ϵ_m . To close the full set of equations, we employ an MHD analog of the familiar von Kármán–Howarth decay law (de Kármán & Howarth 1938; Wan et al. 2012; Bandyopadhyay et al. 2018) for Q_T . Further details on the model, including those on numerical implementation, may be found in Usmanov et al. (2014, 2018).

The simulations have been found to give reasonable agreement with many spacecraft observations of large-scale solar wind fields, turbulence parameters (energy, cross helicity, and correlation scale), and temperature, for varying heliocentric distance and, where feasible, varying heliolatitude (Breech et al. 2008; Usmanov et al. 2011, 2012, 2014, 2016, 2018; Chhiber et al. 2018). The model has been used to compute diffusion coefficients for energetic particles, again finding good agreement with spacecraft observations (Chhiber et al. 2017). Recent work (reviewed below) has combined our model’s output with *STEREO* images to enable a localization of the first $\beta = 1$ surface (Chhiber et al. 2018).

The next section describes various runs of the simulation model performed for this work, and presents results relating to critical surfaces in the solar wind along with predictions along *PSP* orbits.

5. Results

The present work is based on analysis of two classes of simulation runs. (I) In the first case, we employ a dipole magnetic field at the inner boundary, with the dipole tilted at angles of 0° , 5° , 10° , and 30° (Runs I-A, I-B, I-C, and I-D, respectively) relative to the solar rotation axis. A 60° run was also analyzed, but the results were found to be similar to the 30° simulation. This simple configuration has both open (near the pole of the dipole) and closed (near its equator) magnetic field geometry and allows for simulation of both coronal-hole-like and streamer-like flows. This gives us a representation of the ambient, large-scale bimodal solar wind flow during periods of low-to-medium solar activity (McComas et al. 2003; Usmanov & Goldstein 2003; Owens & Forsyth 2013). (II) In the second case, the MHD code is driven by a magnetic field at the base obtained from 1989 July, 1994 July, and 2008 December magnetogram data (Runs II-A, II-B, and II-C, respectively) published by the Wilcox Solar Observatory. Note

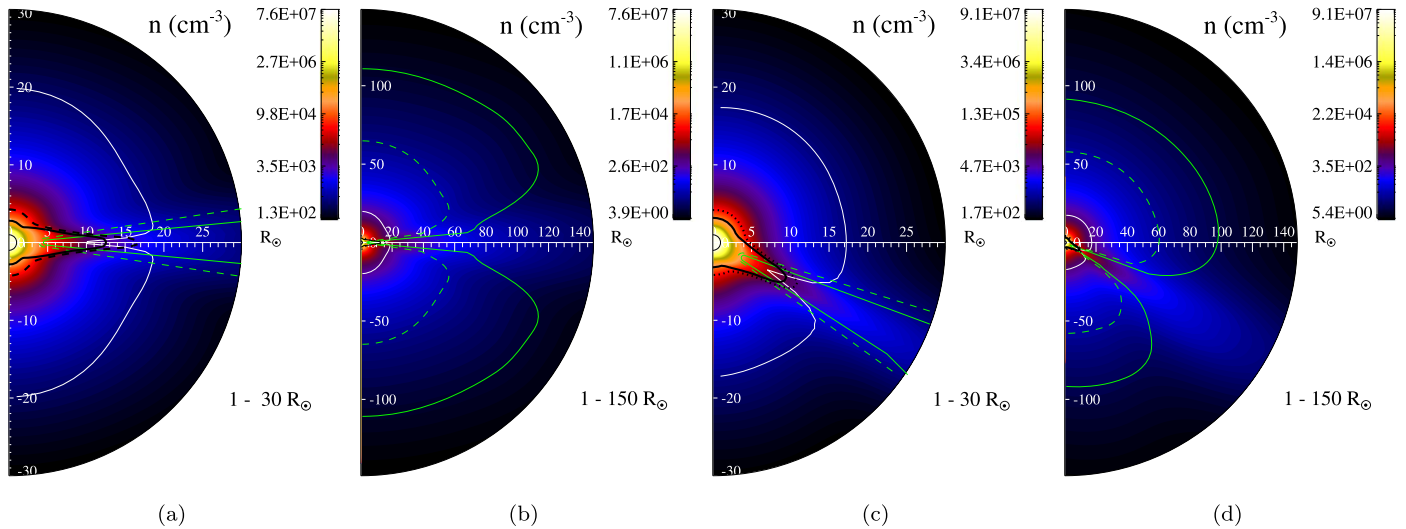


Figure 2. (a), (b) Meridional planes from untilted dipole Run I-A, and (c), (d) 30° tilted dipole Run I-D. Panels (a) and (c) show heliocentric distances from 1 to $30 R_\odot$, while panels (b) and (d) show 1– $150 R_\odot$. The black curves show the sonic surface (solid line using c_s with just proton pressure and dashed line using c'_s , which includes proton and electron pressures; see text), the white curve shows the Alfvén surface, and the green curves show the first unity β surface (solid line shows $\beta_p = 1$ and dashed line shows $\beta_{p+e} = 1$).

that the magnetogram runs use a slightly older numerical model with a simpler WKB-wave-based treatment of the coronal region (1– $45 R_\odot$; see Usmanov et al. 2000, 2014; Usmanov & Goldstein 2003) because the new coronal model (Usmanov et al. 2018) requires further testing with boundary conditions based on solar-maximum magnetograms.

The simulation domain extends from the coronal base at $1 R_\odot$ to 3 au. The following input parameters are specified at the coronal base: the driving amplitude of Alfvén waves ($\sim 30 \text{ km s}^{-1}$), the density ($\sim 1 \times 10^8 \text{ particles cm}^{-3}$), and the temperature ($\sim 1.8 \times 10^6 \text{ K}$). The magnetic field magnitude is assigned either using a source magnetic dipole on the Sun’s poles (with strength 12 G to match values observed by *Ulysses*) or from solar magnetograms. Runs I-A to I-D use an adiabatic index $\gamma = 1.67$ throughout the simulation domain, while Runs II-A to II-C use $\gamma = 1.08$ in the WKB-based coronal region and $\gamma = 1.67$ above $45 R_\odot$. For further numerical details, see Usmanov et al. (2014, 2018).

5.1. Surfaces in the Meridional Plane

The significance of the sonic and Alfvén critical surfaces, as well as the first $\beta = 1$ surface, was discussed in Section 2. Operationally, the Alfvén critical surface is defined by the set of points, scanning outward, at which the solar wind speed first exceeds the Alfvén speed $V_A = B/\sqrt{4\pi\rho}$. Similarly, the sonic surface is defined by the set of points, scanning outward from the Sun, at which the total solar wind speed becomes larger than the sound speed $c_s = \sqrt{\gamma P_p/\rho}$. Here, γ is the polytropic index and P_p is the proton pressure. Another definition of the sound speed is $c'_s = \sqrt{\gamma P/\rho}$, where $P = P_p + P_e$ includes the electron pressure P_e . We show the sonic surfaces computed using both these definitions to stress that the inclusion of various physical effects may change the location of the surface, and it is perhaps more appropriate to envision a transonic region (Lotova et al. 1997) rather than a highly localized surface. Nevertheless, at the fluid level of description, P may be considered the more appropriate measure of pressure.

The plasma beta is also defined in two ways: in terms of the proton beta, $\beta_p = 8\pi P_p/B^2$, and in terms of the total electron plus proton beta, $\beta_{p+e} = 8\pi(P_p + P_e)/B^2$. The first $\beta = 1$ surface is identified as the set of points, scanning outward, at which $\beta = 1$ is first encountered. This is done in the analysis separately for proton beta and for total beta.

Figure 2 depicts the projection of these surfaces onto an arbitrarily selected meridional plane at 37° heliographic longitude for Runs I-A and I-D. Unless specified otherwise, simulation data are plotted in the heliographic coordinate system (HGC; Fränz & Harper 2002). Heliographic latitude is measured from the solar equator positive toward north, and heliographic longitude is defined in the direction of planetary motion, with the XY plane defined by the solar equator.

The surfaces show a laminar appearance and display a very organized ordering. The two configurations depicted are very similar, except for their tilts. The zero tilt case is fully symmetric. For all latitudes well separated from the heliospheric current sheet (HCS), the $\beta = 1$ surface is the most distant, with the Alfvén surface contained well within it, and the sonic surface(s) lower still, in the range $3\text{--}5 R_\odot$. The most dramatic feature is the rearrangement of the surfaces near the heliospheric current sheet region (consistent with previous work that examines the properties of these surfaces, e.g., Pneuman & Kopp 1971; Keppens & Goedbloed 2000; Usmanov et al. 2000; Pinto et al. 2011; Oran et al. 2013), an effect that can completely reverse the surfaces to an opposite ordering. In fact, one can find a substantial region in which the $\beta = 1$ surface lies at lower altitudes than the Alfvén surface. There are also regions, much smaller in these particular cases, in which the sonic surface is found at altitudes above the Alfvén surface. In those small regions, the solar wind would have the somewhat anomalous character of being super-Alfvénic but subsonic. Alfvén wave pressure in such regions may be able to increase the mass flux of the resulting wind at higher radial distances (see Leer et al. 1982).

Before proceeding with further analysis, we want to emphasize that there are unavoidable limitations in using these simulations. One obvious comment is that our MHD solutions are based on simplified data that do not represent the actual

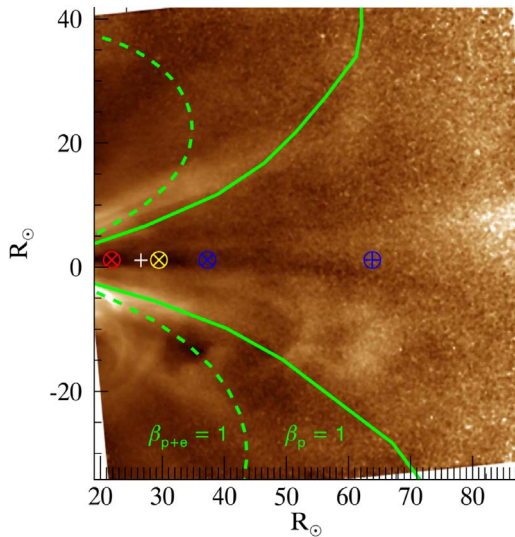


Figure 3. Green curves show the first beta-unity surfaces (solid line for $\beta_p = 1$; dashed line for $\beta_{p+e} = 1$) computed from the model (Run II-C) superimposed on a *STEREO* image from DeForest et al. (2016). The white plus sign shows the location of enhanced turbulence inferred by Lotova et al. (1985; see Figure 5), the *Helios* perihelion is shown as \oplus , and the first three perihelia of the *PSP* are shown as \otimes .

boundary conditions corresponding to the solar wind during the *PSP* passage. More specifically, we emphasize that the discrete spatial resolution of the MHD model limits the thinning of the HCS. Therefore both the HCS and the much wider plasma sheet surrounding it are expected to be broader in the simulation than in the actual solar wind (Winterhalter et al. 1994). A rough estimation based on published data suggests that the real HCS may be a factor of ~ 5 thinner than what we are able to resolve here. Nevertheless, within the resolution parameters of the code, the physics of the simulation is deemed to be accurate, so, for example, the inversion of critical surfaces is expected to occur, albeit over a thinner region, in the solar-minimum conditions seen in some *PSP* orbits.¹⁰

5.2. Remote Sensing Context

We recall briefly the novel use of *STEREO* Heliospheric Imaging (HI) data by DeForest et al. (2016), which examined a series of images of the inner solar wind and argued, based on physical grounds, that the observed striation–foculation transition occurred in the neighborhood of the first plasma- $\beta = 1$ surface. Chhiber et al. (2018) employed MHD simulations, similar to those analyzed here, to provide confirming evidence for this interpretation. Figure 3 revisits this analysis, showing that the region in which the *striae* give way to *foculae* is commensurate with the region in the simulation in which the first $\beta = 1$ surface is encountered, as the wind transitions from magnetic control to hydrodynamic control.

Recently, Kasper et al. (2017) found evidence for a zone, extending from just above the transition region ($\sim 0.3 R_\odot$) to a distance of tens of solar radii, where α -particles are heated preferentially over protons. The lower boundary of this zone would likely be at the chromospheric transition region, where

the plasma collisionality changes from high to weak, thus permitting nonthermal physics to produce observed temperature anisotropies (e.g., Marsch 2006). It is conceivable that this zone of preferential heating ends at the first beta-unity surface, since kinetic temperature anisotropies are generally associated with $\beta \lesssim 1$ (e.g., Matteini et al. 2012). This zone should be detected by the *PSP* when it reaches below the first beta-unity surface.

The location of the sonic critical surface as a function of latitude was estimated from scintillation data by Lotova et al. (1997). Figure 4 shows the Lotova et al. results and compares them with sonic critical surfaces obtained from two MHD simulations: a solar-minimum magnetogram and a solar-maximum magnetogram. We note a reasonable qualitative similarity, especially regarding the oblateness at the poles during solar minimum and the spherical but jagged shape during solar maximum. During solar minimum, there exists a clear demarcation between slow wind streams at equatorial latitudes and fast wind in polar regions. As a result, the wind becomes supersonic at larger distances from the Sun at low latitudes, while the sonic surface at the poles lies at lower heights. These results support the idea that variations in the morphology of the critical surfaces can be used to infer the state of solar activity (e.g., Keppens & Goedbloed 2000; Pinto et al. 2011; Pinto & Rouillard 2017).

Another look at the properties of the solar wind in the critical region is provided by the scintillation intensity data of Lotova et al. (1985), reproduced in Figure 5. For comparison, we show the radial profiles of two parameters obtained from an (axisymmetric) simulation with an untilted dipole (Run I-A), in the ecliptic (Figure 5(a)) and polar (Figure 5(b)) regions. The parameters shown are the radial solar wind speed V_r and the turbulence energy density (per unit mass) Z^2 at 6.75° heliolatitude, representative of the ecliptic region (Figure 5(a)), and at 82° heliolatitude, representative of the polar region (Figure 5(b)). The scintillation profile (measured through $m\nu$, where m is a scintillation index and ν is the frequency of observation; see Lotova et al. 1985) shows a feature in the range $15\text{--}30 R_\odot$ that is interpreted as a region of enhanced turbulence, giving rise to enhanced radio scattering from density irregularities. Shaded regions in Figure 5(a) indicate the range of radii at which the Alfvén and sonic surfaces are found in the ecliptic region in the simulation (between heliolatitudes 6.75° and -6.75°), while the vertical lines in Figure 5(b) represent the locations of these surfaces at 82° heliolatitude. The figure also shows *PSP* perihelia for several orbits. We note that the scintillation feature lies very close to the position of the maximum turbulence energy per unit mass Z^2 from the simulation, and it is also close to the locations of the sonic and Alfvénic critical surfaces in the simulation. This enhancement in turbulence may be caused by the interactions of counterpropagating Alfvén waves (Matthaeus et al. 1999). The acceleration of the wind also begins in this region, with larger speeds and turbulence energies seen at polar latitudes.

5.3. What *PSP* Will See: Dipole-based Simulations

Using the *PSP* trajectory and a coordinate transformation to link it to the global MHD solution, one may graphically illustrate the relationship between the *PSP* orbit and the simulated heliospheric structure. Superposing the orbits on the simulation results should not be construed as a prediction because the boundary data, even if compatible with projected

¹⁰ It would be of interest to compare the present MHD-based results with analyses based on flux-tube solar wind models in which the HCS remains thin (e.g., Pinto & Rouillard 2017). Such a comparison is outside the scope of the present paper.

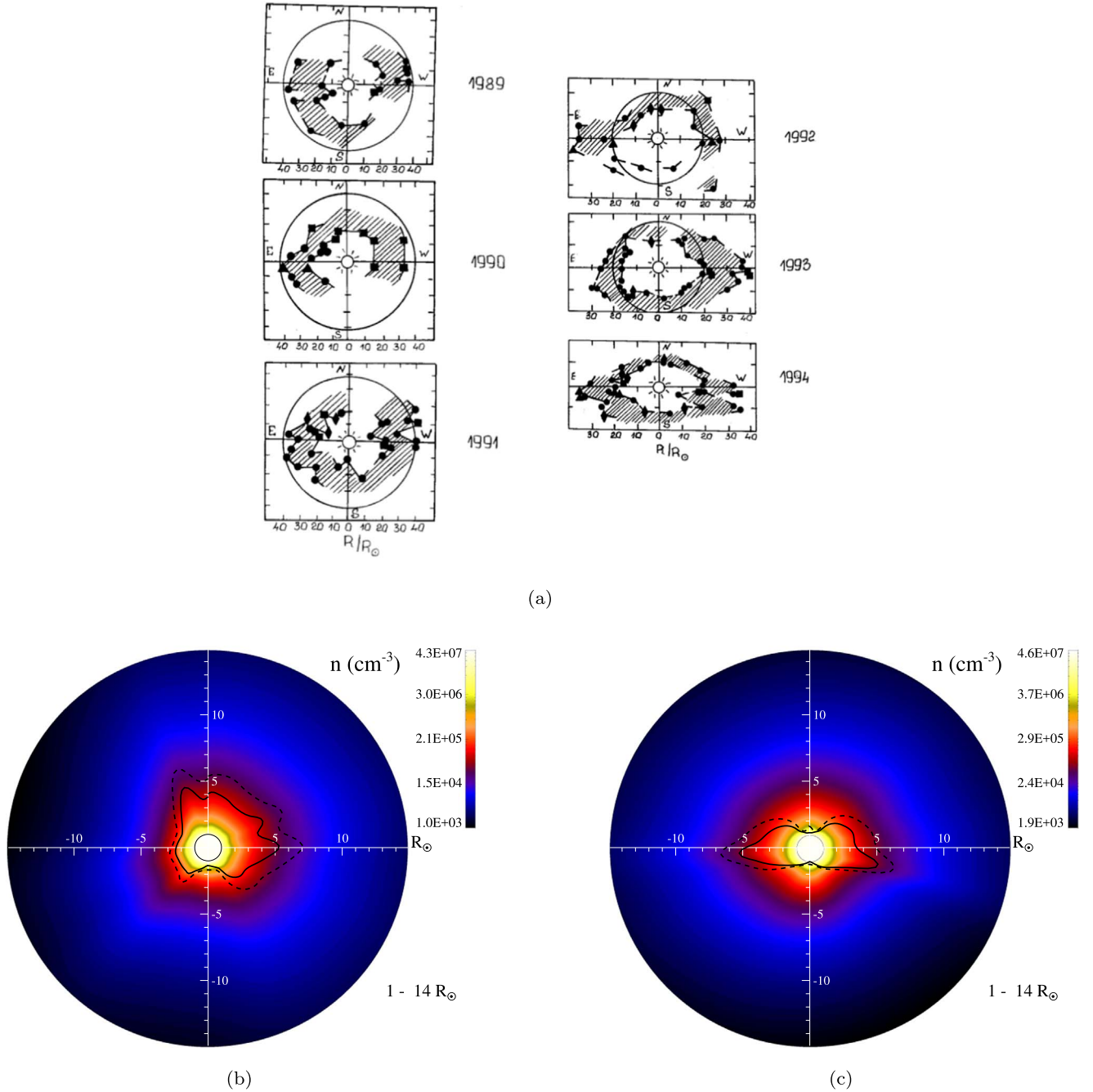


Figure 4. (a) Transonic regions from Lotova et al. (1997), showing the transition from spherically symmetric but jagged morphology at solar maximum (1989), to oblateness at the poles during solar minimum (1994). Sonic surfaces (solid line using c_s with just proton pressure and dashed line using c_s' , which includes proton and electron pressures; see text) from Runs II-A and II-B, using solar maximum (1989 July) and solar minimum (1994 July) magnetograms, respectively. Contours of proton density are shown in the background. The transition from solar maximum (b) to solar minimum (c) is qualitatively consistent with the one seen in Figure 4(a). Reprinted by permission from Kluwer: Springer Nature Solar Physics (Radio Maps of the Solar Wind Transition Region: Lotova et al. 1997).

future conditions, are necessarily imprecise. However, this exercise does present a possible context for the *PSP* mission. Here we evaluate the MHD solution along the *PSP* trajectory, taking solar rotation into account.

To produce an illustrative comparison of the orbits and critical surfaces, we may choose to look at a sequence of (non-inertial) meridional planes that always contain the *PSP* orbit. In this frame, the orientation of the solar dipole field rotates at a nonconstant angular frequency. Figure 6 depicts such a sequence of meridional planes. The MHD simulation used for

this illustration employed a 10° tilted dipole boundary condition (Run I-C), representing solar-minimum conditions likely to be sampled by the *PSP* in its early orbits. The position of *PSP* in each frame (during the eighth orbit; see Figure 8) is at the center of the yellow plus sign. The times are chosen to correspond to *PSP* passing over a critical surface. The plots are labeled by time measured in days from launch. For these conditions, probably not unusual for early *PSP* orbits that occur during solar minimum, the spacecraft is often found skimming the edges of the $\beta = 1$ surface near the HCS. This

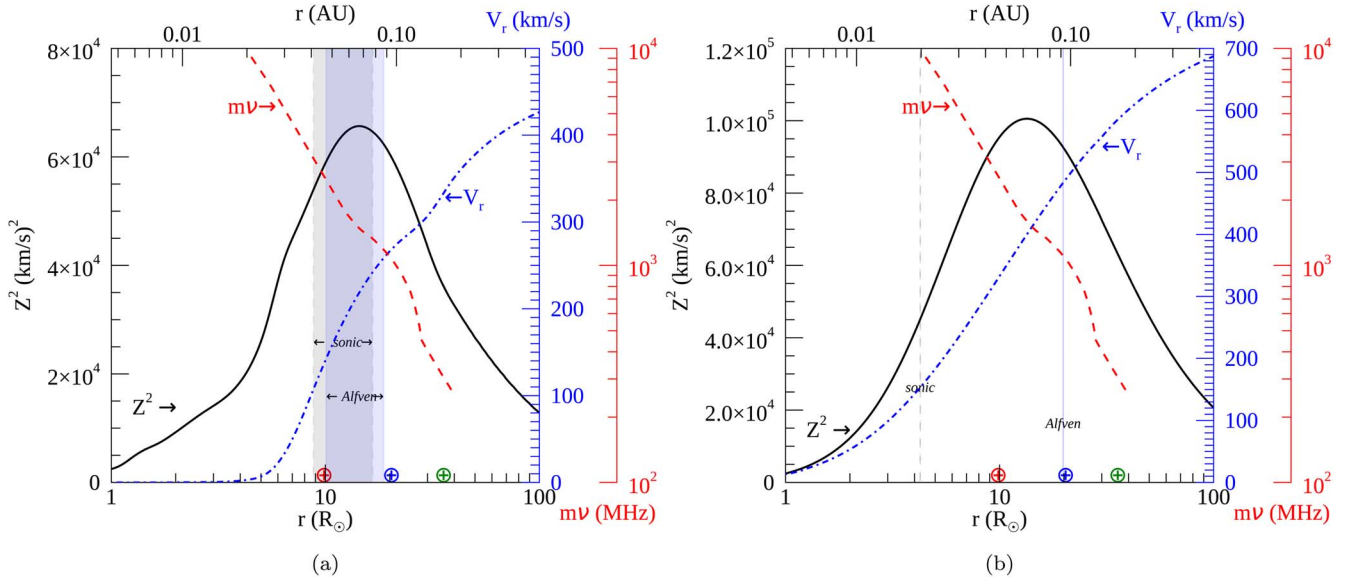


Figure 5. Enhanced scintillation (mv) region from the observations of Lotova et al. (1985), seen as a bump at $\sim 20 R_{\odot}$ in the dashed red curve. Radial solar wind speed V_r (dashed-dotted blue curve) and turbulence energy density (per unit mass) Z^2 (solid black curve) are shown at (a) an ecliptic heliolatitude of 82° and (b) a polar heliolatitude of 82° . Panel (a) shows shaded bands representing the locations of the Alfvén (pale blue band) and sonic (gray band with dashed outline) surfaces in the ecliptic region of the simulation (between heliolatitudes 6.75° and -6.75°). Panel (b) shows vertical lines representing locations of the Alfvén surface (pale blue solid) and the sonic surface (gray dashed) at 82° heliolatitude. All simulation results shown here are from Run I-A. The first, third, and final perihelia of the PSP are represented as \oplus symbols at heliocentric distances of 35.66, 20.35, and $9.86 R_{\odot}$, respectively (Fox et al. 2016).

may provide opportunities for PSP to study $\beta \sim 1$ plasma for extended periods. A video animation of these figures is available with Figure 6. An animation illustrating PSP crossings of critical surfaces in the final orbit, during solar-maximum conditions (Run II-A), is also available.

Another interesting way to visualize the relationship between the PSP orbit and the critical surfaces is to tally the time spent in each orbit within the $\beta = 1$ surface (henceforth β refers to the “two-fluid” plasma beta β_{p+e}), the Alfvén surface, and the sonic surface. For the purposes of the present study, the initial (“launch”) heliolongitude of the PSP is arbitrarily placed within the simulation. Rather than focus on a particular (arbitrary) trajectory, we consider ~ 100 values of the initial longitude $\phi_{PSP,0}$, ranging from 0° to 359° , and perform an average over them. That is, for a given simulation run (that represents a particular type of solar conditions), we first compute the time spent within the critical surfaces during an orbit, for each PSP trajectory defined by a value of $\phi_{PSP,0}$. We then average these times over the different $\phi_{PSP,0}$ values to obtain a mean number of hours within the surfaces, for each orbit. These results are presented in the following figures, discussed below.

As a first example of this compilation, Figure 7(a) shows the residence time within each of these regions, using the planned PSP orbits, for the case of a solar wind with untilted dipole boundary conditions. The upper section of the plot shows, as functions of time, the variation of orbital radial distances, as well as radial position of the critical surfaces at the angular position (heliolatitude and heliolongitude) of the PSP, for an arbitrary $\phi_{PSP,0}$. This directly illustrates PSP’s penetration of the critical surfaces at various times.

Referring to the lower section of Figure 7(a) that shows accumulated time (averaged over $\phi_{PSP,0}$) within critical surfaces, for each orbit, we see that, beginning with orbit 8, this virtual PSP mission penetrates the Alfvén surface for 18 hr or more for all subsequent orbits to 25. Beginning with orbit 10, PSP spends between 15 and 40 hr in each plotted orbit

below the predicted sonic surface. Due to the lack of dipole tilt, an anomalous amount of time is spent in high-beta plasma, and the residence time below the $\beta = 1$ surface is suppressed compared to subsequent cases. Recall also that the HCS in the simulation is artificially wide, and therefore the times spent within the $\beta = 1$ surface are likely to be underestimated, in particular for simulations with low dipole tilts.

Figure 7(b) shows a similar compilation done for a 5° dipole-tilt run. We can see now, as would be expected, that the encounters with critical surfaces have a strong dependence on the dipole tilt angle, which translates into the degree of latitudinal excursion of the HCS. In fact, for this case, the critical surfaces are frequently seen at larger heliocentric distances, with significant consequences for the subcritical-surface residence times. The $\beta = 1$ surface is crossed relatively early, and from orbit 4 onward PSP spends nearly 50 hr or more within it. Furthermore, for all orbits after 7, the PSP spends at least 20 hr within at least one of the critical surfaces. These 20–40 hr periods will represent opportunities for crucial observations. For instance, below the Alfvén surface, the PSP might detect a large population of inward-propagating Alfvén modes, and the enhanced turbulence seen in Figure 5 could be detected in the trans-Alfvénic region.

Two more cases with dipole boundary conditions are shown in Figure 8, with tilt angles of 10° and 30° . The results for a 60° dipole run (not shown) are very similar to the 30° case. It is apparent that the $\beta = 1$ surface is found at considerably larger radial distances as the tilt angle is increased. During solar maximum, the PSP is therefore likely to spend more than a hundred hours under the first beta-unity surface per orbit. Furthermore, Figure 8(b) indicates that no time is spent within the sonic surface during any of the orbits in the 30° dipole case. The reason for this can be understood from the discussion of Figure 4. Since the PSP trajectory stays within low heliolatitudes, it may be able to sample the extended portion of the sonic surface during solar minimum. However, during

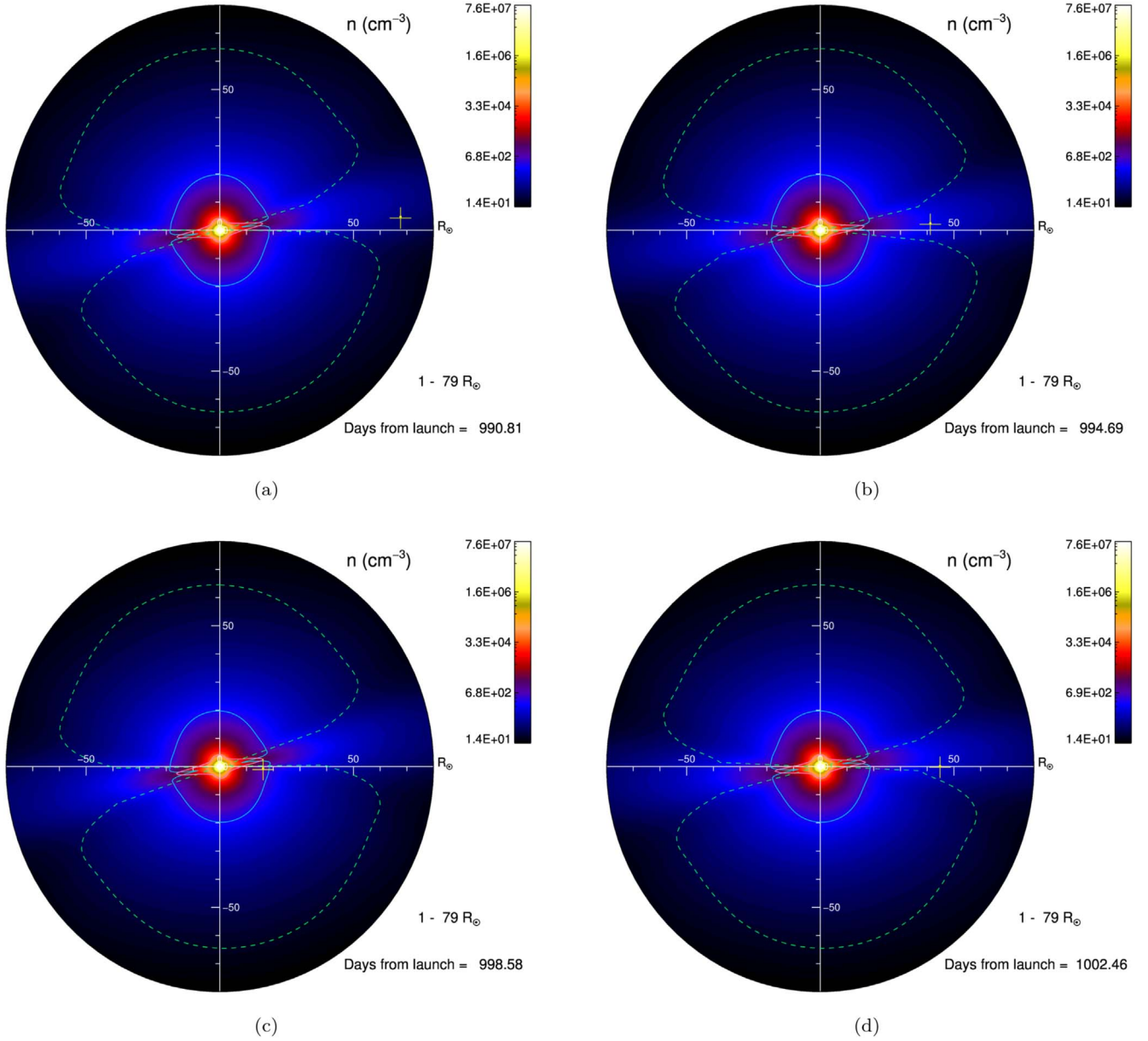


Figure 6. *PSP* crossings of the critical surfaces are illustrated by a sequence of meridional planes that contain the spacecraft trajectory. The eighth orbit is depicted in a 10° dipole simulation (Run I-C; see Figure 8(a)), representing solar-minimum conditions. The sonic, Alfvén, and first (proton+electron) beta-unity surfaces are depicted as solid pink, solid blue, and dashed green curves, which are superposed on contours of proton density. The *PSP* position is at the center of the yellow plus sign. A video animation is available. The top panel of the animation shows the eighth orbit within a 10° dipole simulation (Run I-C) and runs from 983 to 1009 days from launch. The bottom panel of the animation shows the final (24th) orbit within a solar-maximum magnetogram-driven simulation (Run II-A), running from 2498 to 2524 days from launch. The video duration is 7 s.

(An animation of this figure is available.)

solar maximum, the height of this surface is generally too low to be crossed at the latitudes sampled by the spacecraft (see also Figure 2(c)).

5.4. What *PSP* Will See: Magnetogram-based Simulations

Here we briefly show results for two cases in which the MHD simulation is driven by magnetograms: one from solar-minimum conditions (Carrington Rotation 1885, 1994 July; Run II-B; Figure 9(a)) and another from solar-maximum conditions (Carrington Rotation 1818, 1989 July; Run II-A; Figure 9(b)). Examining the solar-minimum case, one sees that the residence times within the Alfvén and sonic surfaces rarely, if ever, exceed 20 hr in a single orbit. Figure 9(b) shows a

solar-maximum case employing a 1989 July magnetogram. The residence times under the $\beta = 1$ surface are below 100 hr during any orbit. There are only a few orbits in which the Alfvén surface is encountered, and then for no more than about 10 hr in a single orbit. As indicated by Figure 9(b) (and Figure 8(b)), *PSP* crossings of the sonic surface are unlikely to occur during solar maximum. A video animation of simulated *PSP* “surface crossings” in the solar-maximum case is available; see Figure 6.

Compared with the dipole-based results (Figures 7 and 8), the reduced time spent under the surfaces in Figure 9 appears to be due to the rapid radial decay of the higher-order multipole magnetic fields that are implied by a complex magnetogram

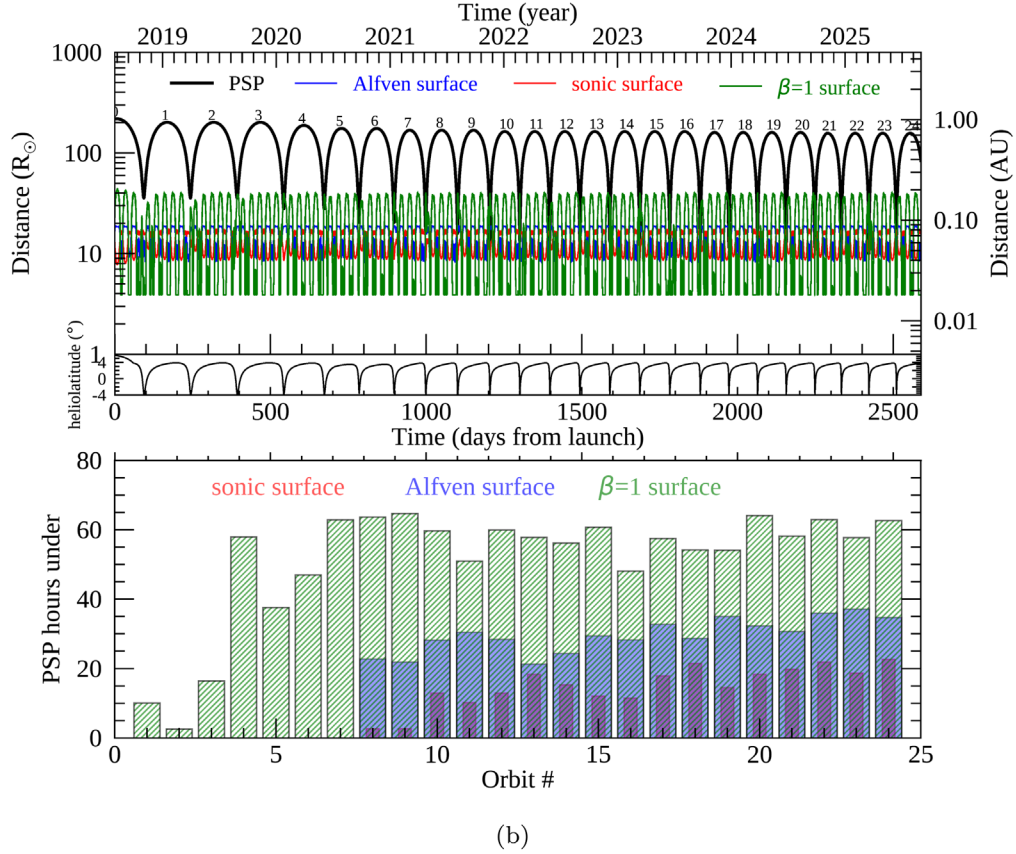
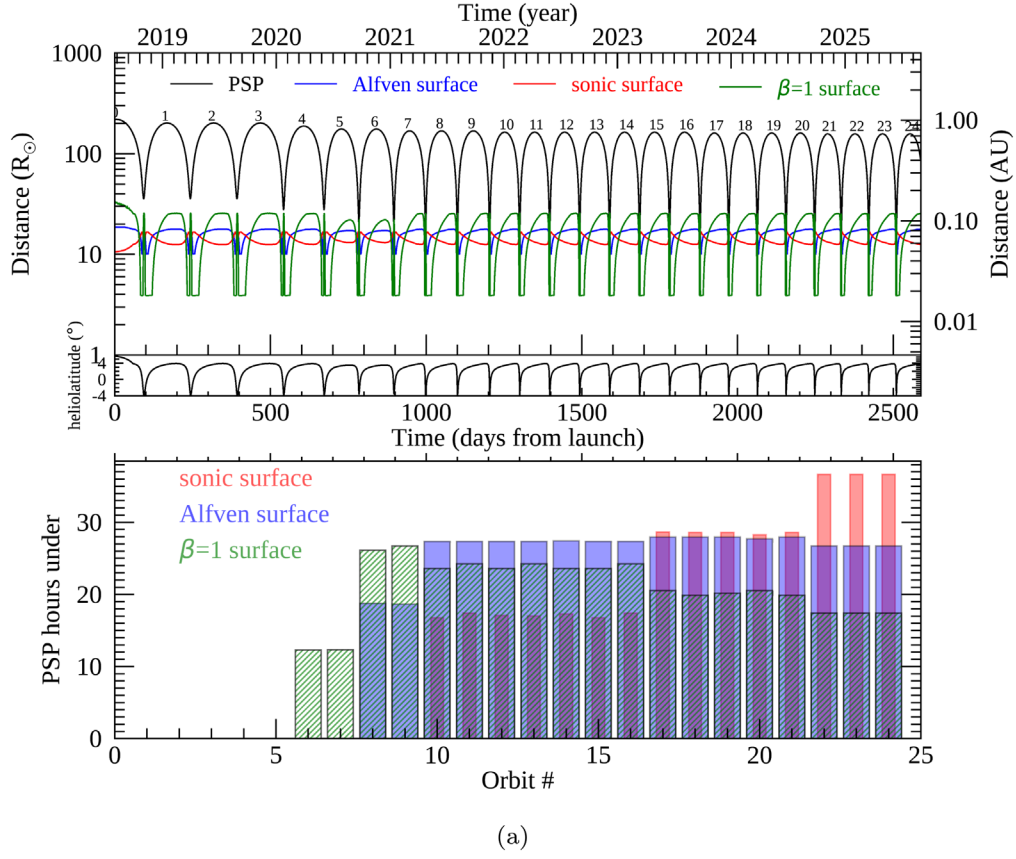
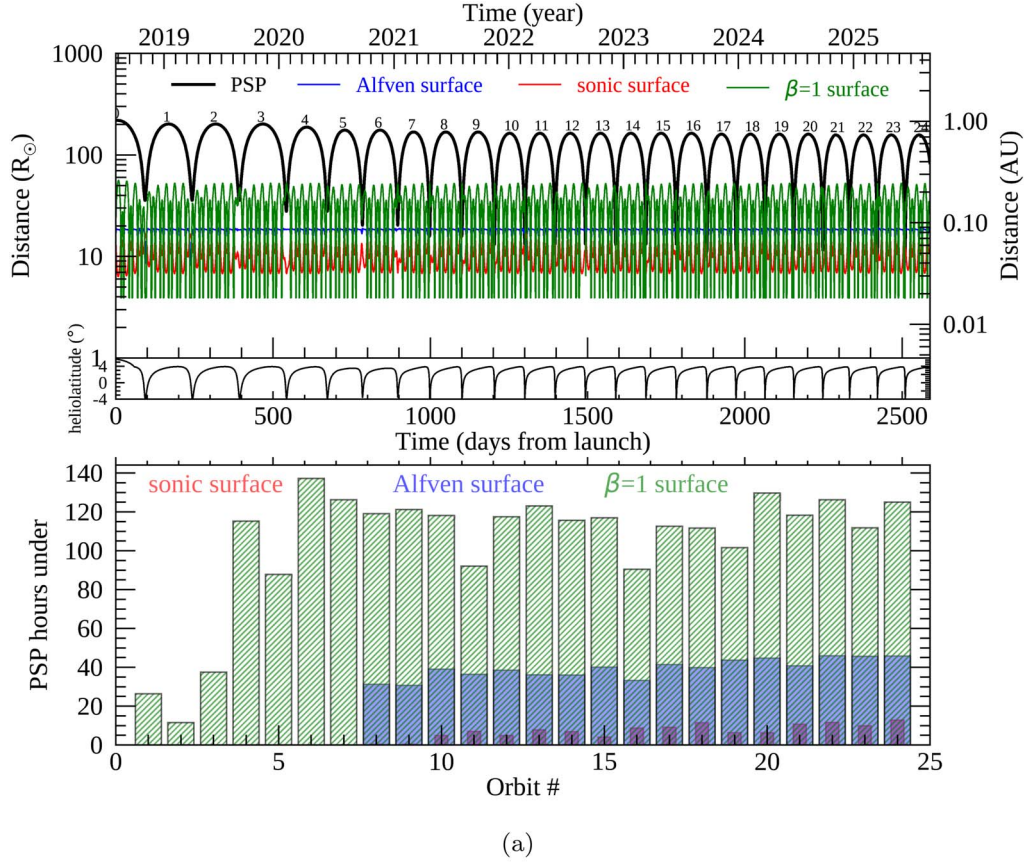
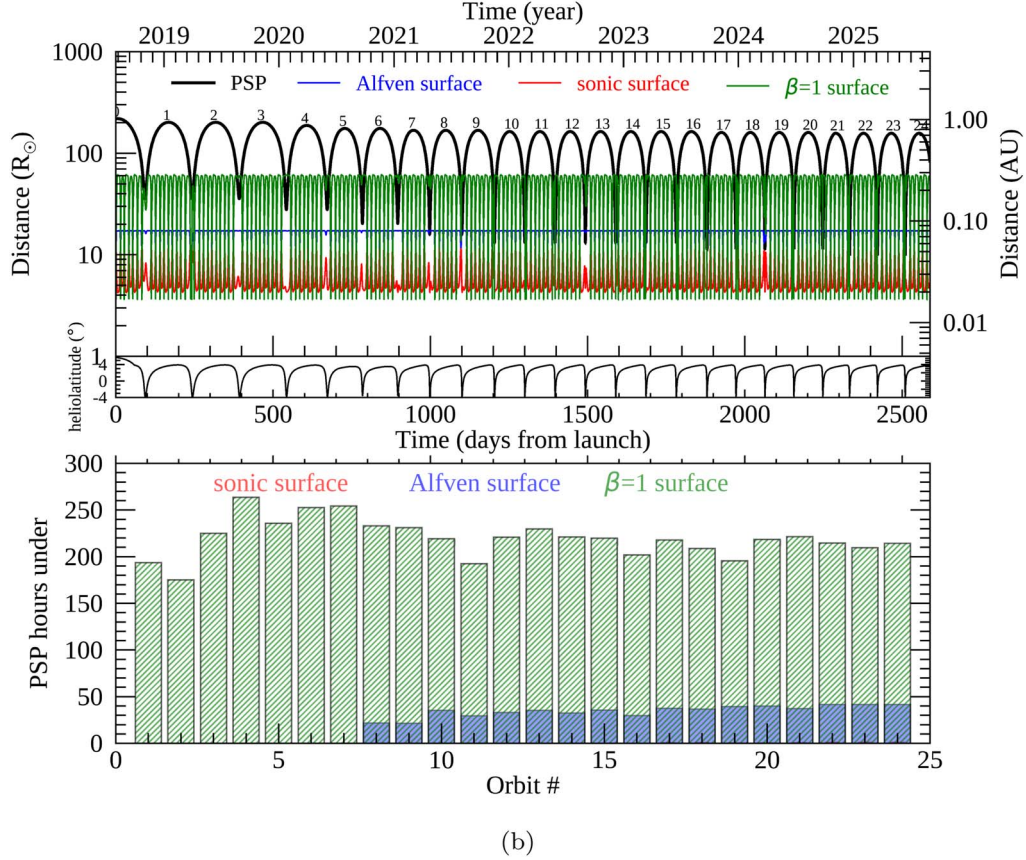


Figure 7. *PSP* surface crossings from simulations with (a) 0° and (b) 5° dipole tilt. In each plot, the top section shows the radial and latitudinal position of the *PSP* for each orbit and the radial position of the critical surfaces at the angular position of the *PSP*. The bottom section shows the time spent by the *PSP* under each surface, per orbit. The striped green, lavender, and narrow red bars represent the $\beta = 1$, Alfvén, and sonic surfaces, respectively.



(a)



(b)

Figure 8. PSP surface crossings from a simulation with (a) a 10° and (b) a 30° dipole tilt. Further description follows Figure 7.

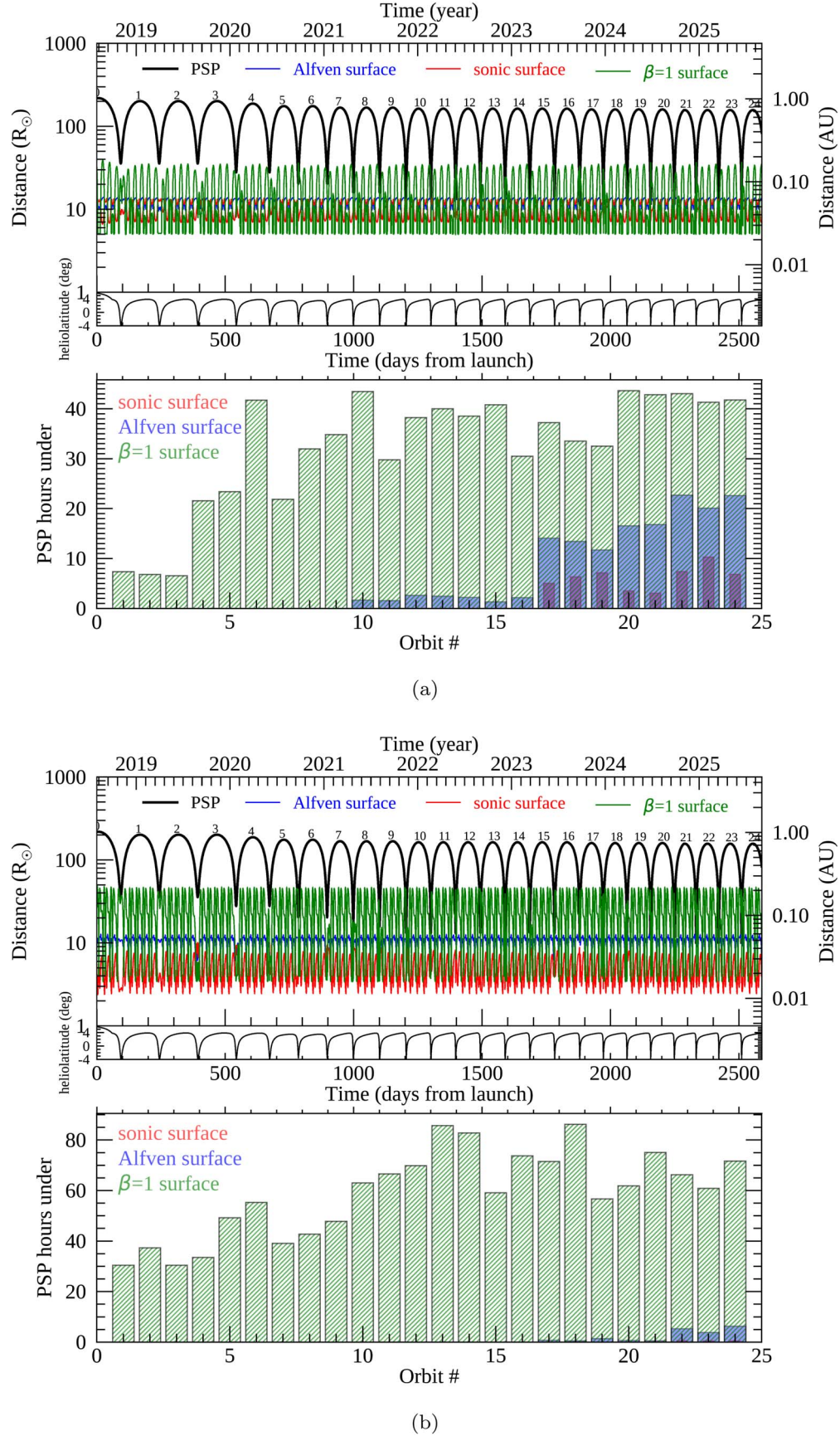


Figure 9. *PSP* surface crossings for (a) a 1994 July (solar minimum) magnetogram run and (b) a 1989 July (solar maximum) magnetogram run. Further description follows Figure 7. A video animation of simulated *PSP* “surface crossings” in the solar-maximum case is available in Figure 6.

boundary condition (Réville et al. 2015). It is also apparent that the *PSP* spends significantly fewer hours within the Alfvén surface in the solar-maximum case (Figure 9(b)), compared to solar minimum (Figure 9(a)). The implied lowering of the Alfvén radius during solar maximum has been noted in other recent work as well (e.g., Pinto et al. 2011; Pinto & Rouillard 2017; Perri et al. 2018).

While the decay of higher-order multipoles is a well-understood effect leading to radial reduction in fine-scale angular structure, this is somewhat offset by dynamical production of fine-scale structure in the corona and beyond. This effect is captured to a certain degree by existing models such as the present one but is also clearly limited by the ability to include fine-scale dynamics, that is, limited by spatial resolution of the numerics (Miesch et al. 2015; Schmidt 2015) as well as by the resolution of the boundary conditions (magnetogram resolution). Accordingly, more realistic global models of the solar atmosphere, like the real corona, will include more fine-scale structure at larger distances, and therefore the possibility of a larger number of brief passages through critical regions that we discuss here. In such cases, interesting modifications might be expected to the depiction in Figure 9 and to its comparison with Figure 8. The “wood grain” structure obtained using high-resolution coronagraph imaging, as discussed by DeForest et al. (2018), hints at the appearance of such fine-resolution structuring in the real solar wind.

6. Conclusions and Discussion

We have shown here some detailed illustrative exercises in the use of a global heliospheric MHD code with turbulence modeling to simulate context that could be observed by the upcoming *PSP* mission. We emphasize again that these results cannot be construed as predictions, since the boundary data employed are not only imprecise but also are not appropriate to the conditions at the time when *PSP* will fly, except perhaps in a qualitative sense. Nevertheless, it is interesting and even useful to explore the kind of conditions that *PSP* might experience, an approach that we call *context prediction*.

In this paper, we have focused on ambient steady-state conditions in the solar wind, driven by boundary conditions that are simple untilted or tilted dipoles, or otherwise magnetograms from previous solar-minimum or solar-maximum epochs. We note that a sensitive parameter is the total solar dipole strength, and we have used values commonly adopted in other work, which lead to agreement with near-Earth observations (Usmanov et al. 2014, 2018; Chhiber et al. 2018), with the understanding that this value is actually not well constrained (Riley et al. 2014; Usmanov et al. 2018).


To summarize, the present results are of two major types. First, we find broad agreement in our study with the interpretation of existing remote sensing results, both from heliospheric imaging and from radio scintillation studies. Our results confirm the likely association of the region near the first outgoing $\beta = 1$ surfaces with morphological changes in the solar wind as observed in *STEREO* imaging (DeForest et al. 2016). Our global simulations also support the idea that a region near the critical Alfvén surfaces may be characterized by a local enhancement of turbulence levels, a feature that may have implications for additional heating and acceleration of the solar wind. Second, the trajectory analyses show that the period of time that *PSP* is likely to spend inside the $\beta = 1$, sonic, and Alfvén surfaces depends sensitively on the degree of solar

activity and the tilt of the solar dipole and the location of the heliospheric current sheet.

Here we have provided a first set of such context predictions, emphasizing the possible range of positions of the sonic and Alfvénic critical surfaces, and the first plasma beta-unity surface. The importance of these surfaces (e.g., Lotova et al. 1985; DeForest et al. 2016; Chhiber et al. 2018) lies in the fact that the physical character and conditions of the interplanetary medium are likely to be different on either side of these boundaries, which may in reality be very complex regions, or at least corrugated surfaces. *PSP* seeks to address questions such as the physical mechanisms that heat the corona and accelerate the wind, and to reveal the structure of the electromagnetic fields, plasma, and energetic particles in these very regions of the corona and wind. Therefore, a baseline understanding of the range of distances at which these regions might be encountered and crossed becomes quite important for anticipating what the mission is likely to measure, for how long, and on which orbits. In a forthcoming paper we will continue these investigations, describing in some detail the turbulence properties that are expected in the regions above and below the critical surfaces and along the *PSP* trajectory (see also Cranmer 2018), together with an evaluation of the validity of the Taylor hypothesis for *PSP* observations.

We thank J. Kasper for useful discussions and the APL *PSP* project office for providing the NASA SPICE kernel containing the *PSP* ephemeris. This research is supported in part by the NASA *PSP* mission through the ISOIS project and subcontract SUB0000165 from Princeton University to University of Delaware, by the NASA HGC program grant NNX14AI63G, by the NASA LWS program under grant NNX15AB88G, and by NASA HSR grants 80NSSC18K1210 and 80NSSC18K1648. The preparation of this article made use of the SAO/NASA Astrophysics Data System (ADS).¹¹

ORCID iDs

Rohit Chhiber  <https://orcid.org/0000-0002-7174-6948>
 Arcadi V. Usmanov  <https://orcid.org/0000-0002-0209-152X>
 William H. Matthaeus  <https://orcid.org/0000-0001-7224-6024>
 Melvyn L. Goldstein  <https://orcid.org/0000-0002-5317-988X>

References

- Bandyopadhyay, R., Oughton, S., Wan, M., et al. 2018, *PhRvX*, **8**, 041052
- Barnes, A. 1979, in Proc. Space Plasma Physics Conf., The Study of Solar-System Plasmas Vol. 2, ed. E. N. Parker, C. F. Kennel, & L. J. Lanzerotti (Washington, DC: National Academies Press), 249
- Bird, M. K., & Edenhof, P. 1990, in Remote Sensing Observations of the Solar Corona, ed. R. Schwenn & E. Marsch (Berlin: Springer), 13
- Boyce, W. E., DiPrima, R. C., & Haines, C. W. 1969, Elementary Differential Equations and Boundary Value Problems, Vol. 9 (New York: Wiley)
- Breech, B., Matthaeus, W. H., Minnie, J., et al. 2008, *JGRA*, **113**, A08105
- Bruno, R., & Carbone, V. 2013, *LRSP*, **10**, 2
- Chhiber, R., Subedi, P., Usmanov, A. V., et al. 2017, *ApJS*, **230**, 21
- Chhiber, R., Usmanov, A., Matthaeus, W., & Goldstein, M. 2016, *ApJ*, **821**, 34
- Chhiber, R., Usmanov, A. V., DeForest, C. E., et al. 2018, *ApJL*, **856**, L39
- Cranmer, S. R. 2018, *RNAAS*, **2**, 158
- Cranmer, S. R., van Ballegoijen, A. A., & Edgar, R. J. 2007, *ApJS*, **171**, 520
- DeForest, C. E., Howard, R. A., Velli, M., Viall, N., & Vourlidas, A. 2018, *ApJ*, **862**, 18
- DeForest, C. E., Howard, T. A., & McComas, D. J. 2014, *ApJ*, **787**, 124
- DeForest, C. E., Matthaeus, W. H., Viall, N. M., & Cranmer, S. R. 2016, *ApJ*, **828**, 66

¹¹ <http://adsabs.harvard.edu/>

- de Kármán, T., & Howarth, L. 1938, *RSPSA*, **164**, 192
- Dmitruk, P., Matthaeus, W. H., Milano, L. J., et al. 2002, *ApJ*, **575**, 571
- Fox, N. J., Velli, M. C., Bale, S. D., et al. 2016, *SSRv*, **204**, 7
- Fränz, M., & Harper, D. 2002, *P&SS*, **50**, 217
- Giordano, S., Antonucci, E., Noci, G., Romoli, M., & Kohl, J. L. 2000, *ApJL*, **531**, L79
- Goldstein, M. L., Roberts, D. A., & Matthaeus, W. H. 1995, *ARA&A*, **33**, 283
- Gombosi, T. I., van der Holst, B., Manchester, W. B., & Sokolov, I. V. 2018, *LRSP*, **15**, 4
- Grall, R. R., Coles, W. A., Klinglesmith, M. T., et al. 1996, *Natur*, **379**, 429
- Gressl, C., Veronig, A. M., Temmer, M., et al. 2014, *SoPh*, **289**, 1783
- Habbal, S. R., Esser, R., Guhathakurta, M., & Fisher, R. R. 1995, *GeoRL*, **22**, 1465
- Hartle, R. E., & Sturrock, P. A. 1968, *ApJ*, **151**, 1155
- Hollweg, J. V. 1974, *JGR*, **79**, 3845
- Hollweg, J. V. 1976, *JGR*, **81**, 1649
- Hundhausen, A. J. 1972, *Coronal Expansion and Solar Wind* (Berlin: Springer), 101
- Isenberg, P. A. 1986, *JGR*, **91**, 9965
- Jacques, S. A. 1978, *ApJ*, **226**, 632
- Kasper, J. C., Klein, K. G., Weber, T., et al. 2017, *ApJ*, **849**, 126
- Keppens, R., & Goedbloed, J. P. 2000, *ApJ*, **530**, 1036
- Klein, K. G., Perez, J. C., Verscharen, D., Mallet, A., & Chandran, B. D. G. 2015, *ApJL*, **801**, L18
- Kopp, R. A., & Holzer, T. E. 1976, *SoPh*, **49**, 43
- Lamers, H. J. G. L. M., & Cassinelli, J. P. 1999, *Introduction to Stellar Winds* (Cambridge: Cambridge Univ. Press)
- Lee, C. O., Luhmann, J. G., Odstrcil, D., et al. 2009, *SoPh*, **254**, 155
- Leer, E., Holzer, T. E., & Fla, T. 1982, *SSRv*, **33**, 161
- Lotova, N. A., Blums, D. F., & Vladimirkii, K. V. 1985, *A&A*, **150**, 266
- Lotova, N. A., Vladimirkii, K. V., & Korelov, O. A. 1997, *SoPh*, **172**, 225
- Makwana, K. D., Zhdankin, V., Li, H., Daughton, W., & Cattaneo, F. 2015, *PhPl*, **22**, 042902
- Marsch, E. 2006, *LRSP*, **3**, 1
- Matteini, L., Hellinger, P., Landi, S., Trávníček, P. M., & Velli, M. 2012, *SSRv*, **172**, 373
- Matthaeus, W. H. 1997, in *AIP Conf. Ser. 385, Robotic Exploration Close to the Sun: Scientific Basis*, ed. S. R. Habbal (Melville, NY: AIP), 67
- Matthaeus, W. H., Oughton, S., Osman, K. T., et al. 2014, *ApJ*, **790**, 155
- Matthaeus, W. H., Wan, M., Servidio, S., et al. 2015, *RSPTA*, **373**, 20140154
- Matthaeus, W. H., Zank, G. P., Oughton, S., Mullan, D. J., & Dmitruk, P. 1999, *ApJL*, **523**, L93
- McComas, D. J., Elliott, H. A., Schwadron, N. A., et al. 2003, *GeoRL*, **30**, 1517
- McKenzie, J. F., Banaszekiewicz, M., & Axford, W. I. 1995, *A&A*, **303**, L45
- Miesch, M., Matthaeus, W., Brandenburg, A., et al. 2015, *SSRv*, **194**, 97
- Monin, A. S., & Yaglom, A. M. 1971, *Statistical Fluid Mechanics: Mechanics of Turbulence* (Cambridge, MA: MIT Press)
- Mullan, D. J. 1990, *A&A*, **232**, 520
- Neugebauer, M., & Snyder, C. W. 1966, *JGR*, **71**, 4469
- Obridko, V. N., & Vaisberg, O. L. 2017, *SoSyR*, **51**, 165
- Oran, R., van der Holst, B., Landi, E., et al. 2013, *ApJ*, **778**, 176
- Owens, M. J., & Forsyth, R. J. 2013, *LRSP*, **10**, 5
- Parashar, T. N., Matthaeus, W. H., Shay, M. A., & Wan, M. 2015, *ApJ*, **811**, 112
- Parker, E. N. 1958, *ApJ*, **128**, 664
- Perri, B., Brun, A. S., Réville, V., & Strugarek, A. 2018, *JPIPh*, **84**, 765840501
- Pinto, R. F., Brun, A. S., Jouve, L., & Grappin, R. 2011, *ApJ*, **737**, 72
- Pinto, R. F., & Rouillard, A. P. 2017, *ApJ*, **838**, 89
- Pneuman, G. W., & Kopp, R. A. 1971, *SoPh*, **18**, 258
- Réville, V., Brun, A. S., Matt, S. P., Strugarek, A., & Pinto, R. F. 2015, *ApJ*, **798**, 116
- Riley, P., Ben-Nun, M., Linker, J. A., et al. 2014, *SoPh*, **289**, 769
- Riley, P., Lionello, R., Linker, J. A., et al. 2015, *ApJ*, **802**, 105
- Roberts, D. A., Goldstein, M. L., Matthaeus, W. H., & Ghosh, S. 1992, *JGR*, **97**, 17
- Schekochihin, A. A., Cowley, S. C., Dorland, W., et al. 2009, *ApJS*, **182**, 310
- Schmidt, W. 2015, *LRCA*, **1**, 2
- Spitzer, L. 1965, *Physics of Fully Ionized Gases* (New York: Interscience)
- Spitzer, L., & Härm, R. 1953, *PhRv*, **89**, 977
- Suzuki, T. K., & Inutsuka, S.-i. 2005, *ApJL*, **632**, L49
- Tu, C.-Y., & Marsch, E. 1995, *SSRv*, **73**, 1
- Usmanov, A. V., & Goldstein, M. L. 2003, *JGRA*, **108**, 1354
- Usmanov, A. V., Goldstein, M. L., Besser, B. P., & Fritzer, J. M. 2000, *JGR*, **105**, 12675
- Usmanov, A. V., Goldstein, M. L., & Matthaeus, W. H. 2012, *ApJ*, **754**, 40
- Usmanov, A. V., Goldstein, M. L., & Matthaeus, W. H. 2014, *ApJ*, **788**, 43
- Usmanov, A. V., Goldstein, M. L., & Matthaeus, W. H. 2016, *ApJ*, **820**, 17
- Usmanov, A. V., Matthaeus, W. H., Breech, B. A., & Goldstein, M. L. 2011, *ApJ*, **727**, 84
- Usmanov, A. V., Matthaeus, W. H., Goldstein, M. L., & Chhiber, R. 2018, *ApJ*, **865**, 25
- van der Holst, B., Sokolov, I. V., Meng, X., et al. 2014, *ApJ*, **782**, 81
- Verdini, A., & Velli, M. 2007, *ApJ*, **662**, 669
- Verdini, A., Velli, M., Matthaeus, W. H., Oughton, S., & Dmitruk, P. 2010, *ApJL*, **708**, L116
- Vourlidas, A., Howard, R. A., Plunkett, S. P., et al. 2016, *SSRv*, **204**, 83
- Wan, M., Oughton, S., Servidio, S., & Matthaeus, W. H. 2012, *JFM*, **697**, 296
- Weber, E. J., & Davis, L., Jr. 1967, *ApJ*, **148**, 217
- Winterhalter, D., Smith, E. J., Burton, M. E., Murphy, N., & McComas, D. J. 1994, *JGR*, **99**, 6667
- Yang, L. P., Feng, X. S., He, J. S., Zhang, L., & Zhang, M. 2016, *SoPh*, **291**, 953